iScience

CellPress
OPEN ACCESS

Article

Co-registration of OPM-MCG signals with CT using optical scanning

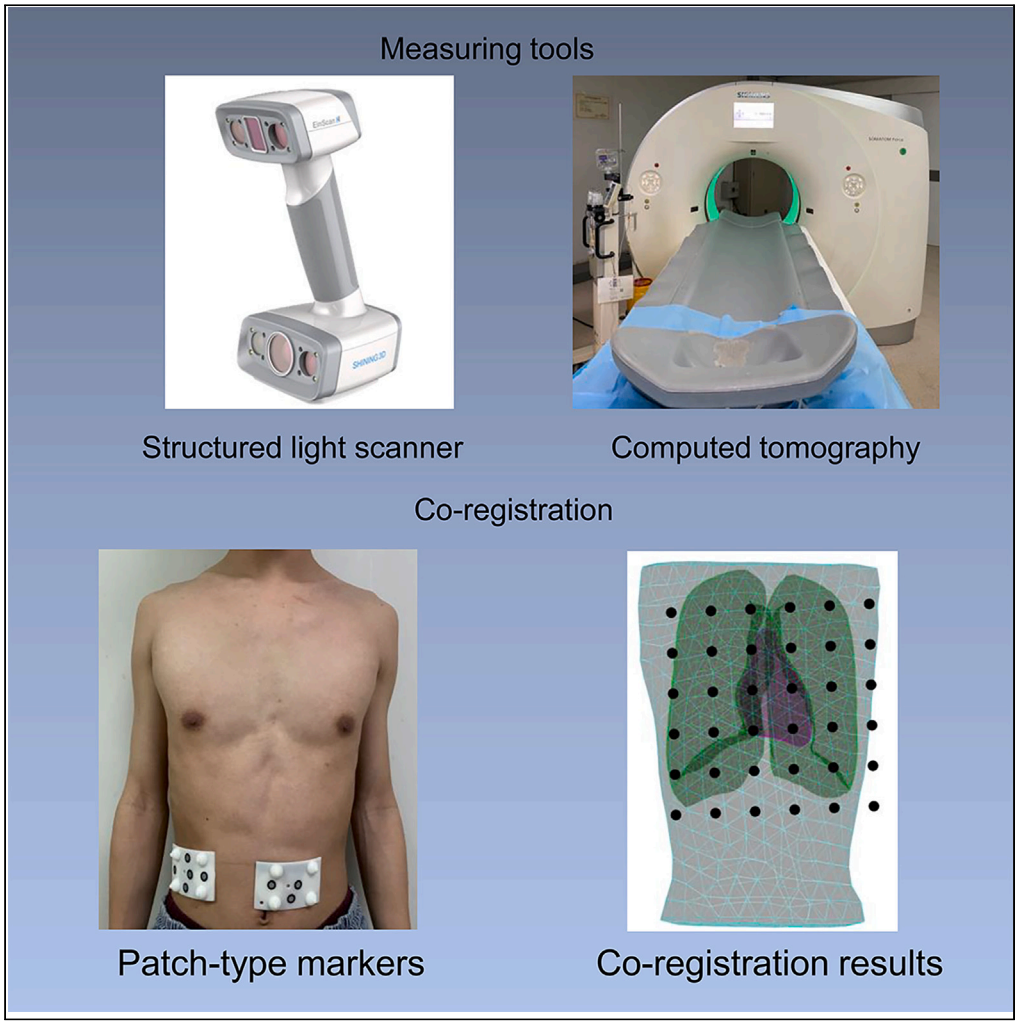

Yanfei Yang, Huidong Wang, Zhanyi Liu, ..., Yang Zhang, Min Xiang, Xiaolin Ning

xiang_min@buaa.edu.cn (M.X.)
ningxiaolin@buaa.edu.cn (X.N.)

Highlights

A magnetocardiography registration method based on structured light scanner is proposed

Improved accuracy of cardiomagnetic registration

A 36-channel OPM-MCG system is constructed

New methodology validated through phantom and human experiments

Yang et al., iScience *26*, 108235
November 17, 2023
https://doi.org/10.1016/j.isci.2023.108235

iScience

CellPress
OPEN ACCESS

Article

Co-registration of OPM-MCG signals with CT using optical scanning

Yanfei Yang,[1,2,3] Huidong Wang,[1,2,3] Zhanyi Liu,[1,2,3] Yanmei Wang,[1,2,3] Xiaole Han,[1,2,3] Yifan Jia,[1,2,3] Jiaojiao Pang,[3,4,5] Fei Xie,[3,4,5] Dexin Yu,[3,5,7] Yang Zhang,[3,5,7] Min Xiang,[1,2,3,6,8,9,*] and Xiaolin Ning[1,2,3,6,8,9,10,*]

SUMMARY

Magnetocardiography (MCG) can be used to noninvasively measure the electrophysiological activity of myocardial cells. The high spatial resolution of magnetic source localization can precisely determine the location of cardiomyopathy, which is of great significance for the diagnosis and treatment of cardiovascular disease. To perform magnetic source localization, MCG data must be co-registered with anatomical images. We propose a co-registration method that can be applied to OPM-MCG systems. In this method, the sensor array and the trunk of the subject are scanned using structured light-scanning technology, and the scan results are registered with the reconstructed structure using computed tomography (CT). This can increase the number of effective cloud points acquired and reduce the interference from respiratory motion. The scanning bed of the OPM-MCG system was modified to be consistent with the CT device, ensuring that the state of the body remains consistent between the cardiac magnetometry measurements and CT scans.

INTRODUCTION

Magnetocardiography (MCG) measures the weak magnetic fields generated outside the body by ion activity within and outside cardiomyocytes and serves as a non-invasive cardiac functional imaging method. Originating in the early 1960s, MCG is currently employed to detect fetal heart magnetism, coronary artery disease, arrhythmias, and other conditions.[1–7] Since the introduction of the superconducting quantum interference device (SQUID) for MCG measurements by Cohen in the 1970s, SQUID-MCG has undergone nearly 50 years of development. However, the requirement for liquid helium to maintain operation results in high maintenance costs and poor equipment flexibility, thereby preventing its widespread adoption. In recent years, optically pumped magnetometer (OPM) sensors have developed rapidly. They can perform ultrasensitive magnetic field measurements at room temperature with low maintenance costs. Compared with SQUID systems, OPM sensors can be placed closer to the signal source, offering a higher signal-to-noise ratio and flexible placement; they have already been applied in MCG.[8–14]

MCG source localization can provide three-dimensional (3D) information of cardiac electrophysiological activity, which can be used for preoperative guidance in cardiac surgery and improved diagnosis of heart disease.[15] To help researchers perform source localization analysis of cardiac electrophysiology, MCG information must be combined with structural imaging to build individualized models. Compared with magnetic resonance imaging (MRI), computed tomography (CT) can rapidly acquire images of the trunk and heart with thin slices and high accuracy and is suitable for building high-precision 3D models of the trunk. Therefore, in this study, we used CT to obtain structural images. However, the MCG and CT data were obtained from different devices. To combine the information from both modalities, the coordinate systems must be registered to determine the accurate position and orientation of the MCG sensors relative to the CT coordinate system.

[1]Key Laboratory of Ultra-Weak Magnetic Field Measurement Technology, Ministry of Education, School of Instrumentation and Optoelectronic Engineering, Beihang University, Beijing 100191, China
[2]Zhejiang Provincial Key Laboratory of Ultra-Weak Magnetic-Field Space and Applied Technology, Hangzhou Innovation Institute, Beihang University, Hangzhou 310051, China
[3]Shandong Key Laboratory for Magnetic Field-free Medicine & Functional Imaging, Institute of Magnetic Field-free Medicine & Functional Imaging, Shandong University, Jinan 250014, China
[4]Department of Emergency Medicine, Qilu Hospital of Shandong University, Shandong Provincial Clinical Research Center for Emergency and Critical Care Medicine, Jinan 250014, China
[5]National Innovation Platform for Industry-Education Intearation in Medicine-Engineering Interdisciplinary, Shandong University, Jinan 250014, China
[6]Hangzhou Institute of National Extremely-weak Magnetic Field Infrastructure, Hangzhou 310028, China
[7]Department of Radiology, Qilu Hospital of Shandong University, Jinan 250014, China
[8]Hefei National Laboratory, Hefei 230088, China
[9]State Key Laboratory of Traditional Chinese Medicine Syndrome, Guangzhou 510006, China
[10]Lead contact
*Correspondence: xiang_min@buaa.edu.cn (M.X.), ningxiaolin@buaa.edu.cn (X.N.)
https://doi.org/10.1016/j.isci.2023.108235

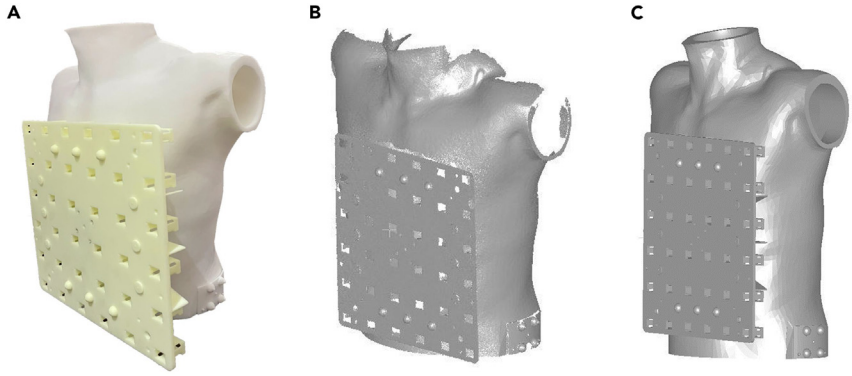

Figure 1. Three models required for prosthetic registration experiments
(A) 3D printed prosthesis model.
(B) Structural light-scanning results.
(C) Prosthesis design diagram.

In a SQUID-MCG system, the coordinates of the positioning coils placed on the subject's skin surface are determined using a position tracker.[16,17] By electrifying the coils and detecting the resulting magnetic field distribution, the locations of the positioning coils relative to the SQUID can be determined. When using the Polhemus (https://polhemus.com/_assets/img/FASTRAK_Digitizer_Brochure.pdf) position tracker, there was no magnetic interference in the surroundings. Operators use a pen-shaped electromagnetic receiver to click on the object being located, which can capture only one point at a time. This results in a small number of location points, a large influence of random errors, and an extended measurement time.[18] In recent years, the technologies have been applied to bioelectromagnetic registration. The rapid development of OPM magnetoencephalography (MEG) has led to the use of optical devices to capture the positions of sensors and markers in MEG registration, with results surpassing those of the Polhemus position tracker.[19–21] Structured light scanners are capable of rapidly acquiring a significant amount of point cloud data. They are not affected by noise from magnetic fields in the external environment during scanning and their registration precision is higher than that of position trackers. OPM-MCG registration has some similarities to OPM-MEG registration. Both methods can achieve high-precision registration through the corresponding relationships. However, magnetocardiographic registration faces greater challenges than magnetoencephalographic registration. The sensor array scanned in MEG registration is helmet-shaped, with a curved surface and rich facial features, which allows for registration using physiological structures such as the nose. However, the sensor array in MCG is flat, and the surface of the torso lacks distinct features with skin morphology that can easily change, making registration more challenging than in MEG. To address the challenge of planar registration, we designed spherical fiducial markers with protrusions on flat sensor array panels to aid registration. Features were added to the trunk skin by designing patch-type markers that were attached to the skin surface and used for both CT and optical scanning, facilitating registration between the optical scanning and CT reconstruction results. Considering that differences in bed-boards could cause changes in skin surface states, we designed a bed-board consistent with the CT device. The layout of the registration markers was optimized to reduce interference from respiratory motion and improve registration accuracy.

In this study, we applied a structured light scanner for the first time to register OPM-MCG with CT. This rapidly determines the coordinates of the sensor array and acquires a larger set of point-cloud data by digitizing both the fiducial markers and the skin surface. Through phantom and human experiments, we validated the accuracy and repeatability of the co-registration method. Additionally, we provide suggestions and precautions for registration for OPM-MCG.

RESULTS

In this study, the repeatability error in the stability of the structured light scanner registration method was verified through phantom experiments, and the position and orientation errors of sensor registration were calculated. Human experiments were conducted to compare the repeatability errors of the structured light scanner in the human experiments. Customized arc-shaped fiducial markers were created to serve as reference points for spatial registration between the different modalities. The bed structure-matching used for CT scanning was produced. Utilizing a consistent bed structure helps achieve spatial alignment between scans.

Phantom experiment and results

This study designed and produced a phantom model that includes a human torso, sensor array panel, and registration markers. The model was 3D printed using photosensitive resin, with a processing precision of $\pm$0.1 mm. The physical model is shown in Figure 1A. To verify the repeatability error of the optical scanner, the phantom model was scanned 10 times using a structured light scanner without moving the phantom. This resulted in a point-cloud set that included the torso and sensor array, as shown in Figure 1B. Simultaneously, we designed a

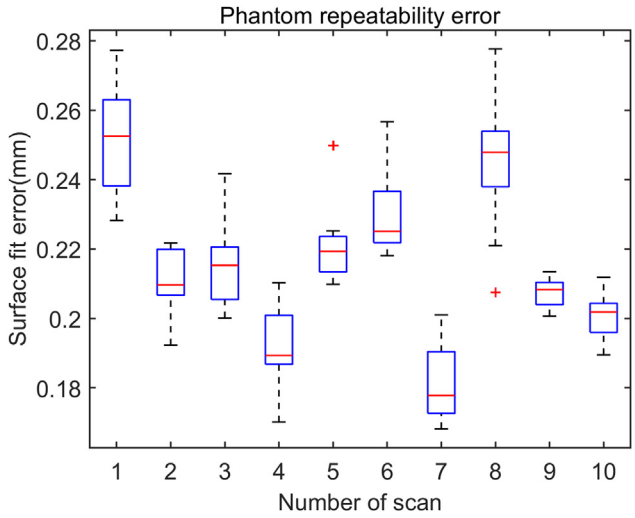

Figure 2. Calculation of the repeatability error based on scans 1–10, respectively

phantom structure diagram to include the actual relative position relationship between the sensor and the torso, which we considered as the ground truth for the subsequent registration, as shown in Figure 1C.

Surface-fitting error

The surface-fitting error was used to evaluate the alignment accuracy of the iterative closest point (ICP) method. It was calculated as the average Euclidean distance between the aligned point cloud and ground truth point cloud. A lower surface-fitting error indicates that the aligned point cloud fits the ground-truth point cloud more accurately. Therefore, the surface-fitting error provides a measure of the alignment accuracy.

Phantom repeatability error

Ten scans were performed on the prosthesis model to evaluate the repeatability and accuracy of the experimental method; 10 repeated scans were performed on the prosthesis model. Each of the 10 scans was used as a reference, and the remaining nine scans were aligned to the reference using the ICP alignment procedure. The distance to its nearest neighbor in the reference scan was calculated for each point in the nine non-reference scans aligned with a particular reference scan. The results are shown in Figure 2. The average fitting errors across the 90 aligned scans ranged from 0.17 mm to 0.28 mm for each reference scan, with an overall mean of 0.21 mm and standard deviation of 0.02 mm. The low repeatability error of 0.21 $\pm$ 0.02 mm obtained by using each scan individually as the reference indicates that the experimental method demonstrates high precision and stability across repeated scans.

Final registration error

The surface-fitting error represents the average distance error between point clouds during registration. The final registration errors refer to the positional and directional errors of the sensor in the CT coordinate system. For the phantom, we know the relative positions and orientations of the sensor and torso during the design phase. This is equivalent to determining the relative position between the sensor and the CT coordinate systems. Assume that there are N sensors; in this experiment, $N = 36$. The true points are $P^{real} = \{p_i^{real}\}, i = 1,\ldots N$, and the points in the CT coordinate system are $P^{CT} = \{p_i^{CT}\}, i = 1,\ldots N$. The true orientation is $o^{real} = \{o_i^{real}\}, i = 1,\ldots N$, and the orientation in the CT coordinate system is $o^{CT} = \{o_i^{CT}\}, i = 1,\ldots N$. The position error P_{final_err} and orientation error θ_{final_err} after calibration are expressed as follows:

$$P_{final\_err} = \frac{1}{N}\sum_{i=1}^{N}\left\|p_i^{real} - p_i^{CT}\right\|_F \quad \text{(Equation 1)}$$

$$\theta_{final\_err} = \frac{\arccos\left(o_i^{real}\cdot o_i^{CT}\right)}{\left|o_i^{real}\right|\left|o_i^{CT}\right|} \quad \text{(Equation 2)}$$

The registration errors of the positions and directions of the sensors are represented by the Euclidean distance and angle, respectively. In this study, we scanned the phantom model 10 times and obtained the average of the 10 registration results. The average position error was 0.72 $\pm$ 0.1 mm (mean $\pm$ STD), and the direction error was 0.15° $\pm$ 0.08°. Figure 3 shows the indicative diagram of position error, where the maximum position error is 1.31 mm, the minimum error is 0.23 mm, and the position errors of the upper sensors were relatively large, which

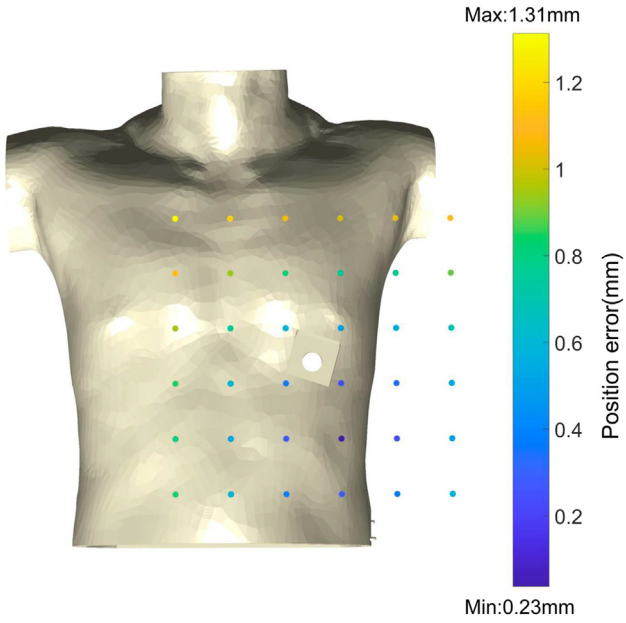

Figure 3. Registration position error corresponding to 36 sensors

may be related to our choice of registration module for the waist markers; the position errors near the markers are smaller, and those at the top are larger. The registration markers were located at the waist. Additionally, the proposed magnetocardiography system fixes the sensor array panel via a cantilever beam structure. However, owing to its own gravitational effects, the panel may experience minor inclination.

Human experiments and results

Human scanning experiments and CT information collection were conducted at the Qilu Hospital of Shandong University. A registration marker was attached to the subject's side, and the subject was placed flat in the supine position on the CT bed. A 320-row CT scan (SOMATOM Force; Siemens, Jinan, China) was used. The CT imaging parameters were prospectively electrocardiogram (ECG)-gated with automatic adjustment of the tube voltage and current. During the diastolic period (79%) of the R-R interval, the layer thickness was 0.05 mm. 3DSlicer (https://www.slicer.org/) was used to segment and reconstruct the CT images.[22]

After the CT scan was completed, the subject was placed in a magnetocardiogram room for heart magnetic signal collection and registration. The human registration experiment was divided into the following three parts. (1) To verify the repeatability error in human experiments, the subject laid flat in the supine position on the magnetocardiogram measurement bed, and the structured light scanner was used to scan the human body and sensor array panel, repeating the scan 10 times. (2) To compare the registration errors of different positions of the attached markers, the subject breathed normally, and the waist and abdominal markers were scanned 10 times. (3) To compare and analyze the effects of different bed-board structures, we designed and fabricated a bed-board with a structure consistent with a CT bed-board. The participants were scanned while lying on their original bed-board. The bed-board was then replaced with a CT-consistent bed-board, and the entire process was repeated for 10 scans. The purpose of this study was to compare the calibration accuracy of the original bed-board and a CT-structured bed-board designed to have consistent structures. This helps analyze the influence of different bed-board structures on the calibration results.

In the human body experiment, we used a structured light scanner to scan the human body and sensor array 10 times. We calculated the reproducibility errors of the waist-side and abdominal calibration modules separately. Figure 4A shows that the reproducibility error for the waist area is 0.37 $\pm$ 0.08 mm. Figure 4B shows that the reproducibility error for the abdominal area is 0.45 $\pm$ 0.09 mm. The results were compared to the repeatability errors of the model, as shown in Table 1. The phantom showed the lowest repeatability error, followed by waist markers, with abdominal markers showing the highest error. This is because the phantom remains perfectly still during scanning, thus, enabling the most stable and consistent scans to be conducted. Compared to body areas impacted by respiration and movement, scanning a static phantom provided the best repeatability. The waist markers were less influenced by human respiration than the abdominal markers and had better stability. Therefore, the reproducibility error for the waist area calibration was lower than that for the abdominal area calibration.

In this experiment, the shapes of the CT and MCG bed-boards were inconsistent. To study the registration errors caused by bed-board differences, we fabricated a bed-board with a curved surface structure consistent with that of the CT device. We conducted a comparative experiment in which the subject was first placed in a supine position on the original electromagnetic bed-board and scanned 10 times. The bed-board was replaced with another bed-board with a curved structure consistent with that of the CT bed-board. The subject laid supine on

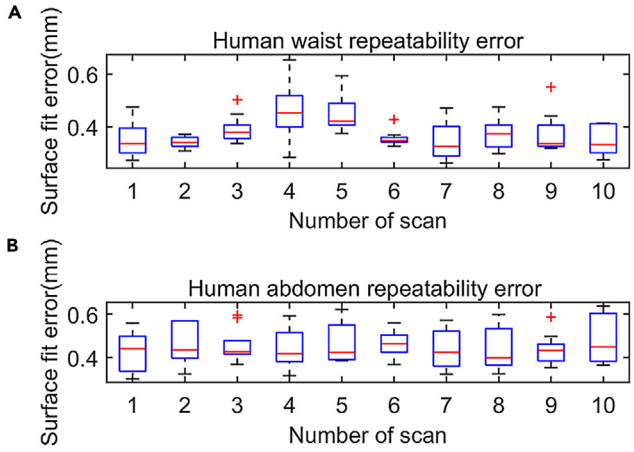

Figure 4. Repeatability error for ten scans

(A) Repeatability error of human waist.

(B) Repeatability error of human abdomen.

a curved bed-board and was scanned 10 times. The 10 sets of scan results from the two bed-boards had a curved structure as the base and a flat structure registered to the curved structure. This was performed to compare the registration accuracy between the inconsistently shaped original bed-board and CT-matched curved bed-board. The surface fitting error between the results of the flat bed-board scans and the curved bed-board scans was 2.62 $\pm$ 0.1 mm. The 10 sets of scan results from the flat and curved structures were registered separately from the reconstructed CT structure. The fitting error for registering the flat structure to CT was 2.94 $\pm$ 0.1 mm, and the fitting error for registering the curved structure on CT was 1.96 $\pm$ 0.1 mm. The registration results show that with the same bed-board structure, the human body morphology is more similar, and the registration results are more accurate. This is because using a bed-board with a curved structure consistent with the CT device helps to simulate the body shape during the CT scan more closely, leading to improved calibration between structured light scanning and CT reconstruction. However, because of the difficulty in maintaining consistent human body states, there was a certain degree of error between the CT-reconstructed torso and the structured light scan results. As shown in Figure 5, in addition to the relatively large fitting errors at the edges, the overall regional fitting error was small, and the structured light-scanning structure was highly consistent with the CT-reconstructed structure. This indicates that although small errors may exist owing to differences in human posture during the scans, the registration between the structured light scans and CT reconstruction was reasonably accurate overall, allowing successful registration of the two modalities.

Based on the aforementioned experiments, we conducted a registration experiment on a bed-board consistent with the CT device and performed structured light scanning. In the human body experiment, we did not have an actual relative positional relationship between the sensors and the CT. We could only use the surface fitting error to represent the calibration error. The registration process in the human body experiment is shown in Figure 6. Figure 6A shows the registration between the sensor array and the torso coordinate system. A coarse registration was performed by selecting 12 markers on the panel, followed by fine calibration using the ICP algorithm, with an ICP error of 0.68 $\pm$ 0.01 mm. Figure 6B shows the transformation process from the torso coordinate system to the CT coordinate system. This involves coarse calibration by selecting eight protruding points from the structured light scan of the markers on the body and their corresponding points from the CT reconstruction. Subsequently, fine calibration was performed by cropping the registration module from the optical scan structure and CT reconstruction, achieving an ICP error of 1.28 $\pm$ 0.01 mm.

The acquired MCG signals contained interference including power line noise and baseline drift. This study employed a combined method consisting of independent component analysis and empirical mode decomposition for signal preprocessing. The preprocessed signals were subsequently averaged to obtain butterfly diagram of the 36-channel MCG signals, as shown in Figure 7A. T-wave timing was selected, and interpolation was performed on the MCG signals at the 36 sensor channel positions to generate magnetic field maps (MFM) under normal physiological conditions, as shown in Figure 7B. The specific MCG preprocessing and imaging methods have been described in previous published literature.[14]

DISCUSSION

OPM-MCG has proven to be applicable for cardiac disease diagnosis and has advantages compared with SQUID-MCG. Registration between CT and MCG is an invisible step in MCG source localization, and the registration accuracy directly affects the source localization accuracy. This study reviewed the registration methods for SQUID-MCG systems. Based on this, registration markers were designed specifically for the OPM-MCG system. They utilize structured light scanning and registration markers to accurately register the measurement data to the CT coordinates. This improved registration approach benefits the clinical application of the OPM-MCG technique.

Table 1. Waist and abdominal repeatability error

Type	Repeatability error (mm)
Waist markers	0.37 ± 0.08
Abdominal markers	0.42 ± 0.09
Phantom	0.21 ± 0.02

To validate the stability of the structured light scanner and obtain the known relative positional relationship between the sensors and CT structure to determine the final sensor position and directional errors, we designed and fabricated a phantom model. Ten scans of the phantom model were conducted to calculate the reproducibility error of 0.21 ± 0.02 mm, which is better than the reproducibility error reported by Zetter et al. in OPM sensor MEG registration,[19] thus proving the stability of this experimental method in OPM-MCG registration. We registered the optical scan results of the phantom to its own structural model, obtaining an average sensor position error of 0.72 ± 0.1 mm and an orientation error of 0.15° ± 0.08°. Compared with the phantom registration error of 4 mm achieved using coils and position trackers in the SQUID-MCG system that was obtained by Mäkelä et al.,[16] our method significantly improved the registration accuracy. We used structured light scanning to acquire point cloud data that were abundant and highly precise. In summary, the high reproducibility and smaller errors achieved in the phantom studies validate the effectiveness and superior accuracy of this registration approach for MCG source localization compared with previous reports.

Adhesive-type registration markers were designed to address the impact of respiration and bed-board differences on MCG registration. Using waist markers for registration yielded a repeatability error of 0.37 ± 0.08 mm, while that for abdominal markers was 0.42 ± 0.09 mm. This is because structured light scanners demonstrate higher accuracy when scanning static objects. The abdominal area is further impacted by human breathing motion and rises and falls more significantly than the waist during breathing. As a result, accurately scanning the abdominal area is more difficult compared to the waist region. Hence, waist markers are better suited for registration purposes. The markers were directly pasted onto the subjects' skin surfaces. Both the structured light scanner and position tracker required bare skin to be exposed to determine the marker positions. Placing markers on the waist allowed female subjects to protect their privacy as it was only necessary to reveal the waist. The fiducial markers were designed using different curvatures according to the waist curves of subjects. For practical utilization, suitable fiducial markers would be selected according to subject physique. In future, fiducial markers could be further improved, for example, their flexible bases could be designed to better fit the human body. Differences in bed-board structures can cause changes in the human body morphology, leading to inconsistencies between CT reconstruction and optical scan results, which can also affect subsequent forward modeling. We designed a bed-board with a consistent structure to keep the human body geometry as consistent as possible and reduce interference from this factor. In summary, this study investigated potential error sources, such as respiration and non-standard bed-boards. The registration markers and customized bed-board helped minimize postural variations between scans, thereby improving the registration accuracy for MCG source localization and modeling.

The Polhemus position tracker costs approximately $8,500 (https://shop.neurospec.com/fastrak). In contrast, the structured light scanner employed in this study costs less than $5,000 (https://www.shining3d.cn/sm/shouchi/EinScanH.html). Considering the costs of commercial applications, structured light scanners are less expensive than position trackers. They also require less time while being able to accurately acquire a large number of data points with precision, independent of operator experience. For example, the Polhemus system requires the operator to manually collect one point individually via pen touch, and point collection precision is dependent on operator skill level. In contrast, a 3-min average scanning time employed in this study enabled automatic acquisition of point cloud data containing millions

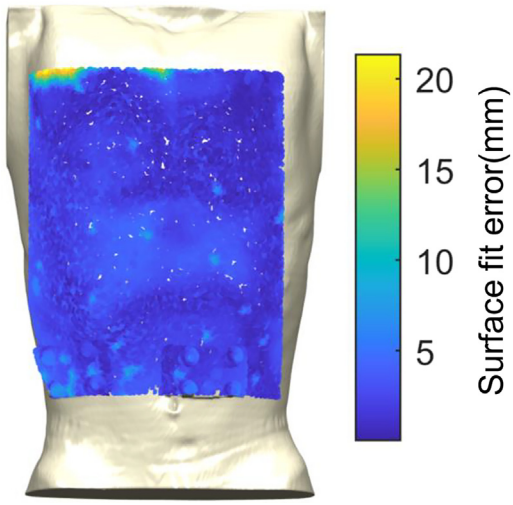

Figure 5. Surface fitting error after registration between the structured light scan results and the CT reconstruction results

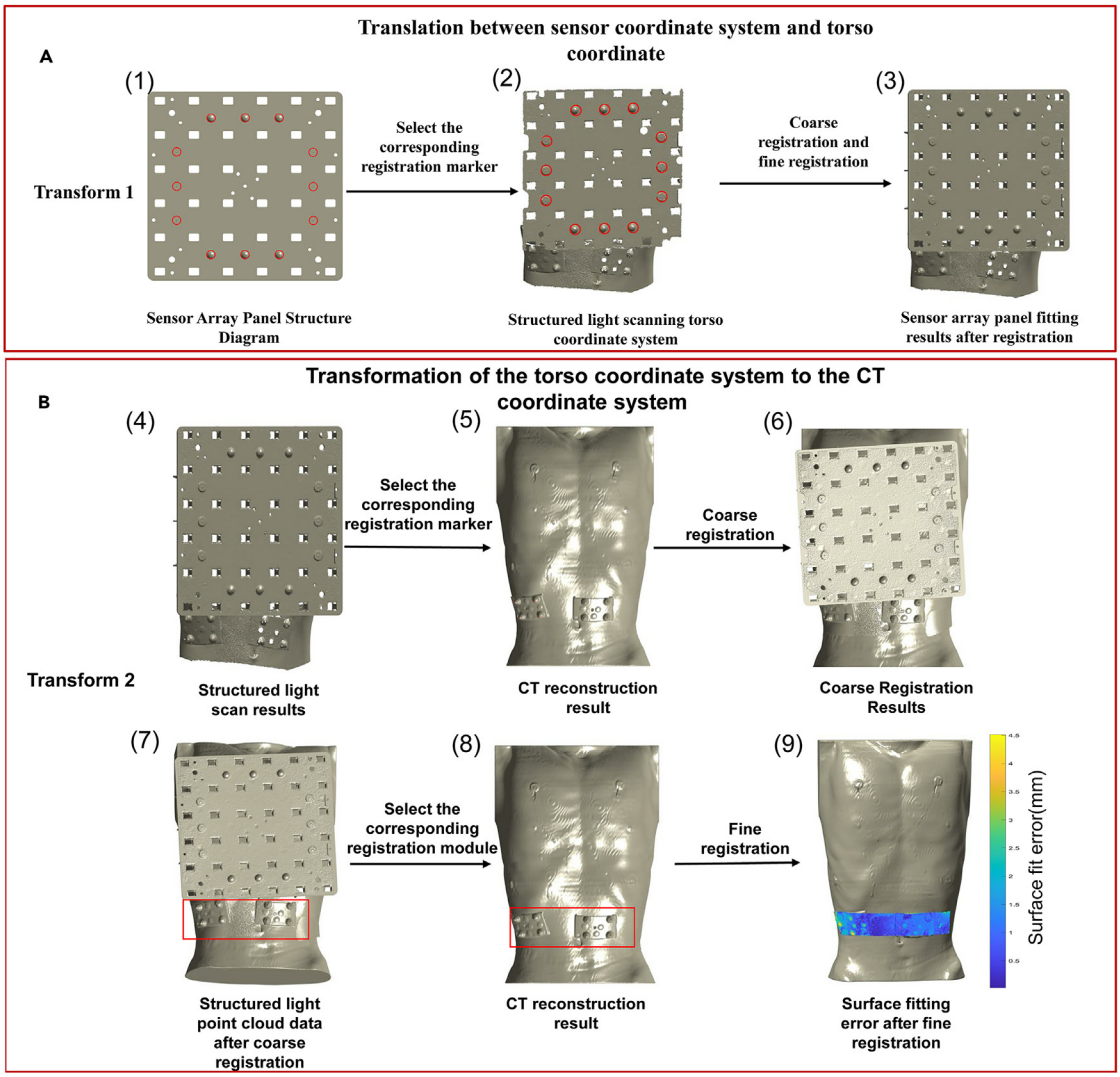

Figure 6. Processing flow of human registration experiment

(A) Transformation of the sensor coordinate system to the torso coordinate system.

(B) Transformation of the torso coordinate system to the CT coordinate system.

of points. In this study, the sensor coordinates were determined before fabricating the sensor array panel; thus, errors may occur in practical applications. Future studies can incorporate calibration experiments to obtain more realistic sensor coordinates, which could further improve registration precision.

Limitations of the study

This study provided a detailed and comprehensive account of the registration workflow of an OPM-MCG system. We designed a reference phantom model to quantify errors from structured light scanning, registration algorithm precision and, ultimately, the registration error between the sensors and CT. In the phantom experiments, the final registration error was used to assess the positional accuracy and orientational registration of the sensors. However, in human studies, the true sensor positions are unknown. Therefore, the surface fitting error is used to evaluate the registration error. However, using the surface fitting error could potentially obscure cases where actual registration accuracy is relatively poor in some local regions. This is because averaging errors across all locations at a global level may mask larger discrepancies that exist at specific points, making overall registration appear more accurate than it actually is across all areas. We distributed the fiducial markers widely, and also visualized registration errors when calculating registration accuracy, to minimize the probability of occurrence of such cases insofar as possible.

Additionally, a human experimental design was optimized using a bed-board having a structure consistent with that of CT and placing markers on the waist to reduce the impact of respiration and bed-board structural differences on registration accuracy. This improved the registration precision of the human experiments. In summary, this study established an enhanced registration methodology for OPM-MCG through phantom and

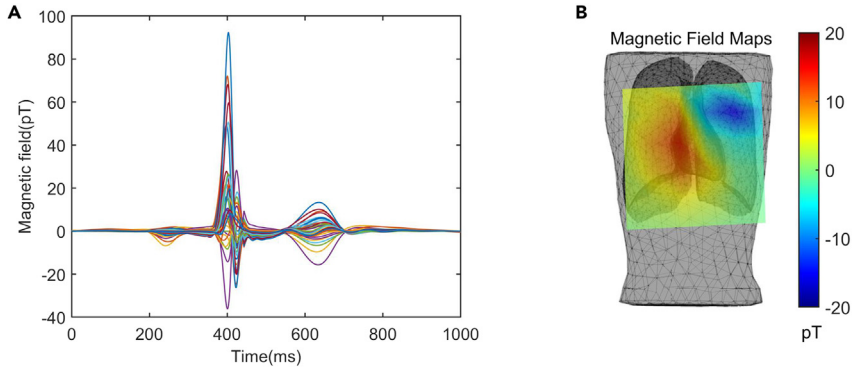

Figure 7. OPM MCG signals

(A) MCG Butterfly diagram.

(B) T peak 36-channel MFMs. Normal MFM has a single dipole structure. The color depth of the figure represents the magnetic field intensity, corresponding to the color bar in the figure.

human validations. The proposed registration procedures and customized experimental set-up represent important advances in achieving accurate MCG source localization. This analysis provides valuable guidance for optimizing real-world MCG applications.

This paper assumes the designed sensor coordinate system represents the true coordinates. However, for actual utilization, the proposed MCG system fixes the sensor array panel using a cantilevered beam structure. The panel may have a slight tilt owing to its own gravity effect. Thus, the actual sensor positions may have slight changes. Calibration experiments should be incorporated to obtain more accurate sensor location coordinates.

STAR★METHODS

Detailed methods are provided in the online version of this paper and include the following:

- KEY RESOURCES TABLE
- RESOURCE AVAILABILITY
  - Lead contact
  - Materials availability
  - Data and code availability
- EXPERIMENTAL MODEL AND STUDY PARTICIPANT DETAILS
  - Human subjects
- METHOD DETAILS
  - OPM-MCG system and coordinate system definition
  - Structured light scanner
  - Registration method
  - Point cloud pre-processing
  - Coarse registration
  - Fine registration

SUPPLEMENTAL INFORMATION

Supplemental information can be found online at https://doi.org/10.1016/j.isci.2023.108235.

ACKNOWLEDGMENTS

This work was supported in part by the Innovation Program for Quantum Science and Technology under grant number 2021ZD0300500, the special fund for basic scientific research business expenses of central universities, the Development and Application of Ultra-Weak Magnetic Measurement Technology based on Atomic Magnetometer under grant number 2022-189-181, the National Natural Science Foundation of China under grant number 62101017, and the Key R&D Program of Shandong Province under grant number 2022ZLGX03.

AUTHOR CONTRIBUTIONS

Conceptualization, Y.F.Y.; Methodology, Y.F.Y.; Software, H.D.W.; Formal analysis. Z.Y.L., Y.M.W., and X.L.H.; Data curation, J.J.P., F.X., D.X.Y., and Y.Z.; Validation, Y.F.J.; Supervision, M.X.; Project administration, X.L.N.; Writing – original draft, Y.F.Y.; Writing – review and editing, X.L.N.

DECLARATION OF INTERESTS

The authors declare that they have no competing interests.

Received: August 24, 2023
Revised: September 28, 2023
Accepted: October 13, 2023
Published: October 17, 2023

REFERENCES

1. Tavarozzi, I., Comani, S., Gratta, C.D., Luzio, S.D., Romani, G.L., Gallina, S., Zimarino, M., Brisinda, D., Fenici, R., and Caterina, R.D. (2002). Magnetocardiography: current status and perspectives. Part II: Clinical applications. Ital. Heart J. *3*, 151–165.
2. Kwong, J.S.W., Leithäuser, B., Park, J.-W., and Yu, C.-M. (2013). Diagnostic value of magnetocardiography in coronary artery disease and cardiac arrhythmias: A review of clinical data. Int. J. Cardiol. *167*, 1835–1842. https://doi.org/10.1016/j.ijcard.2012.12.056.
3. Yamada, S., and Yamaguchi, I. (2005). Magnetocardiograms in Clinical Medicine: Unique Information on Cardiac Ischemia, Arrhythmias, and Fetal Diagnosis. Intern. Med. *44*, 1–19. https://doi.org/10.2169/internalmedicine.44.1.
4. Tantimongcolwat, T., Naenna, T., Isarankura-Na-Ayudhya, C., Embrechts, M.J., and Prachayasittikul, V. (2008). Identification of ischemic heart disease via machine learning analysis on magnetocardiograms. Comput. Biol. Med. *38*, 817–825. https://doi.org/10.1016/j.compbiomed.2008.04.009.
5. Van Leeuwen, P., Voß, A., Cysarz, D., Edelhäuser, F., and Grönemeyer, D. (2012). Automatic identification of fetal breathing movements in fetal RR interval time series. Comput. Biol. Med. *42*, 342–346. https://doi.org/10.1016/j.compbiomed.2011.05.012.
6. Steinisch, M., Torke, P.R., Haueisen, J., Hailer, B., Grönemeyer, D., Van Leeuwen, P., and Comani, S. (2013). Early detection of coronary artery disease in patients studied with magnetocardiography: An automatic classification system based on signal entropy. Comput. Biol. Med. *43*, 144–153. https://doi.org/10.1016/j.compbiomed.2012.11.014.
7. Vairavan, S., Ulusar, U.D., Eswaran, H., Preissl, H., Wilson, J.D., Mckelvey, S.S., Lowery, C.L., and Govindan, R.B. (2016). A computer-aided approach to detect the fetal behavioral states using multi-sensor Magnetocardiographic recordings. Comput. Biol. Med. *69*, 44–51. https://doi.org/10.1016/j.compbiomed.2015.11.017.
8. Han, X., Xue, X., Yang, Y., Liang, X., Gao, Y., Xiang, M., Sun, J., and Ning, X. (2023). Magnetocardiography using optically pumped magnetometers array to detect acute myocardial infarction and premature ventricular contractions in dogs. Phys. Med. Biol. *68*, 165006. https://doi.org/10.1088/1361-6560/ace497.
9. Tao, R., Zhang, S., Wang, Y., Mi, X., Ma, J., Shen, C., and Zheng, G. (2022). MCG-Net: End-to-End Fine-Grained Delineation and Diagnostic Classification of Cardiac Events From Magnetocardiographs. IEEE J. Biomed. Health Inform. *26*, 1057–1067. https://doi.org/10.1109/JBHI.2021.3128169.
10. Livanov, M.N., Koslov, A.N., Sinelnikova, S.E., Kholodov, J.A., Markin, V.P., Gorbach, A.M., and Korinewsky, A.V. (1981). Record of the human magnetocardiogram by the quantum gradiometer with optical pumping. Adv. Cardiol. *28*, 78–80. https://doi.org/10.1159/000391945.
11. Bison, G., Wynands, R., and Weis, A. (2003). A laser-pumped magnetometer for the mapping of human cardiomagnetic fields. Appl. Phys. B *76*, 325–328. https://doi.org/10.1007/s00340-003-1120-z.
12. Alem, O., Sander, T.H., Mhaskar, R., LeBlanc, J., Eswaran, H., Steinhoff, U., Okada, Y., Kitching, J., Trahms, L., and Knappe, S. (2015). Fetal magnetocardiography measurements with an array of microfabricated optically pumped magnetometers. Phys. Med. Biol. *60*, 4797–4811. https://doi.org/10.1088/0031-9155/60/12/4797.
13. Strand, S., Lutter, W., Strasburger, J.F., Shah, V., Baffa, O., and Wakai, R.T. (2019). Low-Cost Fetal Magnetocardiography: A Comparison of Superconducting Quantum Interference Device and Optically Pumped Magnetometers. J. Am. Heart Assoc. *8*, e013436. https://doi.org/10.1161/JAHA.119.013436.
14. Yang, Y., Xu, M., Liang, A., Yin, Y., Ma, X., Gao, Y., and Ning, X. (2021). A new wearable multichannel magnetocardiogram system with a SERF atomic magnetometer array. Sci. Rep. *11*, 5564. https://doi.org/10.1038/s41598-021-84971-7.
15. Aita, S., Ogata, K., Yoshida, K., Inaba, T., Kosuge, H., Machino, T., Tsumagari, Y., Hattori, A., Ito, Y., Komatsu, Y., et al. (2019). Noninvasive Mapping of Premature Ventricular Contractions by Merging Magnetocardiography and Computed Tomography. JACC. Clin. Electrophysiol. *5*, 1144–1157. https://doi.org/10.1016/j.jacep.2019.06.010.
16. Mkel, T., Ltjnen, J., Sipil, O., Lauerma, K., and Magnin, I.E. (2001). Error Analysis of Registering of Anatomical and Functional Cardiac Data Using External Markers (AGU Spring Meet).
17. Mäkelä, T., Pham, Q.C., Clarysse, P., Nenonen, J., Lötjönen, J., Sipilä, O., Hänninen, H., Lauerma, K., Knuuti, J., Katila, T., and Magnin, I.E. (2003). A 3-D model-based registration approach for the PET, MR and MCG cardiac data fusion. Med. Image Anal. *7*, 377–389. https://doi.org/10.1016/S1361-8415(03)00012-4.
18. Zetter, R., Iivanainen, J., Stenroos, M., and Parkkonen, L. (2018). Requirements for Coregistration Accuracy in On-Scalp MEG. Brain Topogr. *31*, 931–948. https://doi.org/10.1007/s10548-018-0656-5.
19. Zetter, R., Iivanainen, J., and Parkkonen, L. (2019). Optical Co-registration of MRI and On-scalp MEG. Sci. Rep. *9*, 5490. https://doi.org/10.1038/s41598-019-41763-4.
20. Cao, F., An, N., Xu, W., Wang, W., Yang, Y., Xiang, M., Gao, Y., and Ning, X. (2021). Co-registration Comparison of On-Scalp Magnetoencephalography and Magnetic Resonance Imaging. Front. Neurosci. *15*, 706785. https://doi.org/10.3389/fnins.2021.706785.
21. Cao, F., An, N., Xu, W., Wang, W., Li, W., Wang, C., Xiang, M., Gao, Y., and Ning, X. (2023). Optical Co-Registration Method of Triaxial OPM-MEG and MRI. IEEE Trans. Med. Imag. *42*, 2706–2713. https://doi.org/10.1109/TMI.2023.3263167.
22. Fedorov, A., Beichel, R., Kalpathy-Cramer, J., Finet, J., Fillion-Robin, J.-C., Pujol, S., Bauer, C., Jennings, D., Fennessy, F., Sonka, M., et al. (2012). 3D Slicer as an image computing platform for the Quantitative Imaging Network. Magn. Reson. Imaging *30*, 1323–1341. https://doi.org/10.1016/j.mri.2012.05.001.
23. Xie, X., Zhou, X., Zhao, F., Wang, W., and Sun, J. (2022). Optimization of a High Screening Performance and Low Noise Magnetically Shielded Cylinder for SERF Atomic Magnetometer. IEEE Sensor. J. *22*, 20373–20380. https://doi.org/10.1109/JSEN.2022.3208424.
24. Rusu, R.B., Marton, Z.C., Blodow, N., Dolha, M., and Beetz, M. (2008). Towards 3D Point cloud based object maps for household environments. Robot. Autonom. Syst. *56*, 927–941. https://doi.org/10.1016/j.robot.2008.08.005.
25. Pomerleau, F., Colas, F., Siegwart, R., and Magnenat, S. (2013). Comparing ICP variants on real-world data sets: Open-source library and experimental protocol. Aut. Robots *34*, 133–148. https://doi.org/10.1007/s10514-013-9327-2.
26. Arun, K.S., Huang, T.S., and Blostein, S.D. (1987). Least-Squares Fitting of Two 3-D Point Sets. IEEE Trans. Pattern Anal. Mach. Intell. PAMI- *9*, 698–700. https://doi.org/10.1109/TPAMI.1987.4767965.
27. Oostenveld, R., Fries, P., Maris, E., and Schoffelen, J.-M. (2011). FieldTrip: Open Source Software for Advanced Analysis of MEG, EEG, and Invasive Electrophysiological Data. Comput. Intell. Neurosci. *2011*, 156869. https://doi.org/10.1155/2011/156869.
28. Sinko, M., Kamencay, P., Hudec, R., and Benco, M. (2018). 3D Registration of the Point Cloud Data Using ICP Algorithm in Medical Image Analysis. In 2018 ELEKTRO (IEEE), pp. 1–6. https://doi.org/10.1109/ELEKTRO.2018.8398245.

STAR★METHODS

KEY RESOURCES TABLE

REAGENT or RESOURCE	SOURCE	IDENTIFIER
Software and algorithms		
3D Slicer	Fedorov et al. (2012)[22]	https://www.slicer.org/
Fieldtrip v20230303	Oostenveld et al. (2011)[27]	https://www.fieldtriptoolbox.org/download/
MATLAB vR2022b	MathWorks	https://ww2.mathworks.cn/products/matlab.html
Co-registration algorithm	This paper	https://doi.org/10.5281/zenodo.8376520
Other		
Human subjects	This paper	N/A

RESOURCE AVAILABILITY

Lead contact

Further information and requests for resources and reagents should be directed to and will be fulfilled by the lead contact, Xiaolin Ning (ningxiaolin@buaa.edu.cn).

Materials availability

This study did not generate new unique reagents.

Data and code availability

- All data reported in this article will be shared by the lead contact on request.
- All original code has been deposited at Zenodo and is publicly available as of the date of publication. DOIs are listed in the key resources table.
- Any additional information required to reanalyze the data reported in this article is available from the lead contact on request

EXPERIMENTAL MODEL AND STUDY PARTICIPANT DETAILS

Human subjects

The patient is a 24-year-old adult male of Asian descent. The participant provided written informed consent for the experimental procedure, which was conducted in accordance with the Declaration of Helsinki and was reviewed and approved by the Ethics Committee of Scientific Research of Shandong University Qilu Hospital.

METHOD DETAILS

OPM-MCG system and coordinate system definition

The MCG study was conducted at the Magnetocardiography Laboratory of Qilu Hospital, Shandong University, China. A 36-channel OPM-MCG device was used for the experiments, which consists of a semi-open cylindrical magnetic shielding device, a data acquisition and control unit, an OPM array, and a cardiogram image processing unit (see Figure S1).

Second generation zero-field OPM sensors (QuSpin) were used (https://quspin.com/products-qzfm/). The sensor's size is 2.4 × 16.6 × 24.4 mm^3, and it is connected to the control unit via a 6.5-m cable. The theoretical noise level is 7–10 fT/√Hz, normal operation requires background noise less than 50 nT, and the dynamic range is ±5 nT. To meet the requirement of less than 50 nT background noise for normal OPM operation, we custom-designed a multilayer semi-open cylindrical magnetic shielding barrel to shield against external magnetic field interference. The shielding barrel was composed of four layers of mu-metal and one layer of aluminium. The gap between the 4 layers of mu-metal was 20 mm. The outermost aluminium casing is capable of shielding the external high-frequency electromagnetic field while protecting the inner metal layers from pressure.[23] The innermost layer had a diameter of 800 mm and a length of 1600 mm. The working area was 600–800 mm from the bottom of the barrel and the maximum residual magnetism inside the barrel was less than 10 nT. The background noise in the semi-open cylindrical magnetic shielding cylinder is shown in Figure S2. OPM sensors were controlled by a sensor control and data acquisition system (Art Technology PXI chassis, Art, China). This system can simultaneously acquire data from 36 channels at a 1 kHz sampling frequency.

A rigid array panel with 36 sensor slots was designed. The array panel was 3D printed with photosensitive resin, offering an accuracy of ±0.1 mm. To avoid signal cross-talk between sensors, the centre spacing between OPM sensors was set to 55 mm. Sensors were arranged in a 6 x 6 array, covering a measurement area of 300 x 300 mm. This area was sufficient to encompass the heart and to meet the magnetocardiography measurement requirements. The positions and orientations of the sensors within the sensor-array coordinate system were determined during the design of the array panel. Based on the physical structure of the sensor array, the position of each sensor was defined as the centre of the top surface of each slot, 17.9 mm downwards, which was the centre of the sensitive element chamber of the sensor. Because of the difficulty of flat-plane registration, 12 markers for registration were designed at symmetrical positions on the outer surface of the sensor array panel. Owing to the difficulty of panel alignment, 12 alignment mark points were designed at symmetrical locations on the outer surface of the sensor array panel. The marked points include hemispherical protrusions with a diameter of 15 mm at the top and bottom and cylindrical protrusions with a diameter of 15 mm and a height of 3 mm on the left and right sides. As shown in Figure S3A, the centre point of the sensor array panel was defined as the origin. The positive X-axis is perpendicular to the array panel and upwards from the origin, the Y-direction is towards the cylindrical markers, and the Z-direction is towards the spherical markers. In the OPM-MCG system, the participants lay supine below an array panel. After adjusting the distance between the sensor array panel and participant's chest, a coordinate system is established based on the participant's torso. As shown in Figure S3B, the torso coordinate system originates at the midline between the breasts, with head-to-toe as the positive X-axis, right-to-left of the body as the positive Y-axis, and upwards perpendicular to the XY plane as the positive Z-axis. The CT coordinate system can uniquely locate the spatial position of each 3D point in CT images, providing a frame of reference for medical image processing and analysis. As shown in Figure S3C, the position of the xiphoid process was set as the origin of the coordinates. The positive X-axis is perpendicular to the participant's frontal surface, the positive Y-axis is from the participant's right-to-left along the coronal plane, and the positive Z-axis is upwards towards the participant's head.

Structured light scanner

We used an industrial-grade handheld dual-light source colour 3D scanner (EinScan H, Shining 3D, Hangzhou, China) that can quickly scan objects and display the results in real time. The reference working distance was 470 mm, the scanning depth of the field was 200–700 mm, and the highest scanning accuracy was 0.05 mm. It can be operated single-handedly and simultaneously, satisfying the requirements for scanning human markers and sensors. The structured light scanner was calibrated prior to scanning. During the scanning process, the scanner adjusts the optimal distance from the scanned object in real time and moves slowly to ensure continuous integration of the 3D measurement results. The scanner automatically aligns continuous image frames to reduce the impact of object movement. The average scanning time was 3 min. To obtain clearer results, the scan results were further reconstructed using EXScan software after the scanning was complete.

Registration method

The purpose of the alignment is to determine the position and orientation of the sensors relative to the CT scan. For the OPM-MCG system, the alignment involves a two-step transformation among the three coordinate systems to obtain the locations of the sensors within the CT coordinate system. The registration process, shown in Figure S4, proceeds as follows. The sensor-array coordinate system contains information regarding the position and orientation of the sensors, which is determined during the design. The torso coordinate system contains information for the relative position of the human body and sensors obtained by scanning with a structured-light scanner. The CT coordinate system contains information regarding the physiological structure of the human body, obtained by segmentation and reconstruction after a CT scan. The sensor array panel contains 12 protruding marker points. By matching the corresponding marker points between the sensor array and torso coordinate systems, a rotation matrix and translation vector (R_{S-T}, T_{S-T}) can be determined to transform the sensor array information into the torso coordinate system. The torso and CT coordinate systems were aligned using the waist alignment marker points. These marker points consist of arced stickers that are adhered to the participants' waist and contain four hemispherical protrusions on the top surface. By aligning the marker points, rotation and translation matrices (R_{T-C}, T_{T-C}) are used to transform the torso coordinate system into a CT coordinate system. This ultimately provides the relative position and orientation of the sensors with respect to the CT scan, thereby completing the alignment.

The overall process of the registration algorithm is shown in Figure S5 and is divided into three parts: point cloud pre-processing, coarse registration, and fine registration. The principles and significance of these three aspects are detailed in the following subsections.

Point cloud pre-processing

The point cloud obtained from the structured light scanner contains a background that must be removed to isolate the target object. After segmenting out the object, there remain isolated noise points around the target. These noise points can make it difficult to accurately estimate local features of the point cloud, such as surface normals and curvature, potentially increasing the alignment error.[24] Isolated noise points are typically removed using spatial decomposition techniques (e.g. *k*-d tree) and using the 3D Euclidean distance as a metric to search for the nearest neighbours. For each point p_i in the point set $P = \{p_i, i = 1, \ldots N\}$, the average d_i and standard deviation σ_i of the distances to the k nearest neighbours in the set $Q = \{q_j, j = 1, \ldots k\}$ are calculated as follows:

$$d_i = \frac{\sum_{j=1}^{k} q_j - p_i}{k} \quad \text{(Equation 3)}$$

$$\sigma_i = \sqrt{\frac{1}{k}\sum_{j=1}^{k}\left(q_j - d_i\right)^2} \quad \text{(Equation 4)}$$

Outlier points with distances outside the range of $d_i \pm \alpha \times \sigma_i$ are removed, where the value of α depends on the size of the analysed neighbourhood. A trade-off exists between the threshold and k value. Smaller α and larger k values may achieve stronger denoising effects, albeit also risk losing more detail. Conversely, a larger α and smaller k value may retain more detail, albeit some noise points may also be retained .We set $k = 10$ and $\alpha = 1$, which are validated on our datasets, to effectively remove isolated noise points, with approximately 1% of the points considered as isolated noise points, as shown in Figure S6.

Point cloud data obtained from structured light scanning contain huge amounts of data with millions of points. To facilitate subsequent alignment and improve the computational efficiency, the point cloud data are downsampled. A voxel grid is constructed by assigning points in the point cloud data to the voxels. Adjacent voxels are grouped and merged using an octree, and the geometric centre of each group of proximate voxels is calculated to represent that group.[25] These representative points serve as downsampled point cloud data, which can preserve the local and global geometric structures of the point cloud data while significantly reducing the number of points.

Coarse registration

If the point-to-point correspondence between two datasets is fully known, then the alignment problem can be easily solved. However, because the point cloud data that we actually process do not have this property, estimating the initial correspondence becomes critical. The first step in the alignment is to compute the initial alignment and determine the correspondences that can be used to transform the source point cloud into the convergence region of the target. For a small set of points with known correspondences, the transformation can be solved directly using least-squares optimisation.[26] We add alignment markers to all three coordinate systems with protruding vertices on the markers for easy manual selection. Based on the feature points of the alignment markers, the transformation matrices between the coordinate systems can be solved directly to perform a coarse alignment.[27] As shown in Figure 1, considering the alignment between the torso and CT coordinate systems as an example, the protruding points of the markers are manually selected while performing the transformation between the two coordinate systems. The marker point set in the torso coordinate system is A and that in the CT coordinate system is B, where A and B both contain n points $A = \{a_i\}, i = 1, \ldots n$ and $B = \{b_i\}, i = 1, \ldots n$, respectively, which are 3×1 column vectors. The goal of least-squares alignment is to find a rotation matrix R (3 × 3 matrix) and translation vector T (3 × 1 column vector) that minimise the sum of squared distances between corresponding points in point sets A and B. The objective function can be expressed as

$$\min\{R, T\} = \sum \|b_i - (Ra_i + T)\|^2 \quad \text{(Equation 5)}$$

To solve for R and T, the centroids of point sets A and B are computed:

$$A\_center = \frac{1}{n} * \sum_{i=1}^{n} a_i \quad \text{(Equation 6)}$$

$$B\_center = \frac{1}{n} * \sum_{i=1}^{n} b_i \quad \text{(Equation 7)}$$

The centroids are subtracted from the points to obtain centred point sets:

$$A' = A - A\_center \quad \text{(Equation 8)}$$

$$B' = B - B\_center \quad \text{(Equation 9)}$$

The covariance matrix H between the centred point sets is computed as:

$$H = \sum_{i=1}^{n} A' B'^{T} \quad \text{(Equation 10)}$$

The covariance matrix H is decomposed using singular value decomposition (SVD):

$$H = U \Sigma V^T \quad \text{(Equation 11)}$$

The optimal rotation matrix is

$$R = VU^T \quad \text{(Equation 12)}$$

The translation vector is:

$$T = B\_center - RA\_center \quad \text{(Equation 13)}$$

We substitute the solved rotation matrix R and translation vector T into Equation 5, which minimises the average distance between the two point-clouds. Least-squares alignment determines the optimal alignment between two point sets by minimising the sum of squared errors. It finds a transformation that minimises the distance between the corresponding points.

Fine registration

Structured light scanning obtains a large amount of point cloud data, which requires rapid iterations and approximate solutions for point-cloud registration. The iterative closest point (ICP) algorithm is a commonly used point-cloud registration method.[28] Its goal is to find a rotation matrix R and translation vector T through iterative optimisation to minimise the average distance between the two point clouds; it is suitable for the registration between large point clouds. After coarse alignment is performed on the point clouds, the corresponding marker points are selected from the point clouds in the two coordinate systems. An iterative rigid transformation is then calculated based on these marker points and is finally applied to the entire point cloud to achieve fine alignment. The iterative process refines the initial transformation computed from the coarse alignment. The optical scan point cloud of the torso is represented as $P_t = \{p_t^i\}, i = 1,\ldots n_t$, and the CT-reconstructed point cloud is represented as $P_c = \{p_c^i\}, i = 1,\ldots n_c$, where $p_t^i = (p_t^{ix}, p_t^{iy}, p_t^{iz})$ and $p_c^i = (p_c^{ix}, p_c^{iy}, p_c^{iz})$ are 1×3 row vectors. During the ICP registration process, the rotation matrix R and translation vector T obtained by least-squares registration are set as the initial values, and the number of iterations is represented by k. The ICP algorithm operates by constantly iterating and performing the following operations at each iteration:

a. For each point p_t^i in the source point cloud, find the closest point p_c^i in the target point cloud. Speed up the search using the k-d tree nearest neighbour search;
b. Compute the transformation (R_k, T_k) that minimizes the distances between all matched point pairs;
c. Transform all points in the source point cloud using (R_k, T_k);
d. Compute the error for this iteration by calculating the average Euclidean distance between the points in the source and target point clouds.

If the error is below a threshold, or the maximum number of iterations is reached, the current (R_k, T_k) transformations are output as the final result; otherwise, another iteration is performed to further improve the alignment.